AIP | Journal of Applied Physics

Thermal analysis of high intensity organic light-emitting diodes based on a transmission matrix approach

Xiangfei Qi and Stephen R. Forrest

Citation: J. Appl. Phys. **110**, 124516 (2011); doi: 10.1063/1.3671067
View online: http://dx.doi.org/10.1063/1.3671067
View Table of Contents: http://jap.aip.org/resource/1/JAPIAU/v110/i12
Published by the AIP Publishing LLC.

Thermal analysis of high intensity organic light-emitting diodes based on a transmission matrix approach

Xiangfei Qi[1] and Stephen R. Forrest[1,2,a)]
[1]*Department of Physics, University of Michigan, Ann Arbor, Michigan 48109, USA*
[2]*Department of Electrical Engineering and Computer Science and Department of Materials Science and Engineering, University of Michigan, Ann Arbor, Michigan 48109, USA*

(Received 30 August 2011; accepted 16 November 2011; published online 27 December 2011)

We use a general transmission matrix formalism to determine the thermal response of organic light-emitting diodes (OLEDs) under high currents normally encountered in ultra-bright illumination conditions. This approach, based on Laplace transforms, facilitates the calculation of transient coupled heat transfer in a multi-layer composite characteristic of OLEDs. Model calculations are compared with experimental data on 5 cm × 5 cm green and red-emitting electrophosphorescent OLEDs under various current drive conditions. This model can be extended to study other complex optoelectronic structures under a wide variety of conditions that include heat removal via conduction, radiation, and convection. We apply the model to understand the effects of using high-thermal-conductivity substrates, and the transient thermal response under pulsed-current operation. © *2011 American Institute of Physics*. [doi:10.1063/1.3671067]

I. INTRODUCTION

Organic light-emitting diodes (OLEDs) have attracted attention due to their high efficiency, broad color gamut, ease of fabrication, and mechanical flexibility when deposited on plastic or metal foil substrates.[1,2] A particular challenge in achieving intense OLED sources for illumination or other applications is to efficiently remove heat that can accelerate degradation of the organic active materials under the high currents required. This is a particular problem for large area devices where Joule heating can be substantial,[3,4] leading to a pronounced temperature rise during operation. An example of such heating is the electrophosphorescent stacked red-green-blue OLED that has been demonstrated as a high intensity white lighting source.[5] At a current density of 40 mA/cm^2 and an operating voltage of 10 V, the optimized device demonstrates a luminance of 10 000 cd/m^2, corresponding to a power efficiency (*PE*) of 12 lm/W. This leads to a power dissipation of 4 kW/m^2 that can result in a temperature rise in excess of 30 °C.

Since localized Joule heating degrades the efficiency, operational lifetime,[6] and brightness uniformity,[7] it is important to quantitatively understand the thermal environment of the multilayer composite device under high current operation, and then to mitigate the effects of heating by optimized device and system design guided by this understanding. In this work, we calculate the thermal properties of OLEDs using an approach based on transmission matrix analysis that is generally applicable to complex multilayer structures. Laplace transforms are used to determine the response of the system to the combined effects of thermal radiation, conduction, and convection, while also taking into account the non-dissipative energy loss through OLED light emission. Our approach is an extension of the heat-transfer method introduced by Pipes[8] used to analyze heat flow across insulating walls, however, in our approach we include: (i) parallel and series pathways required for accurate consideration of losses by the combined processes of thermal convection, conduction, and radiation, (ii) thermal generation within the layers themselves, (iii) losses through light emission, (iv) heat flow across interfaces with finite thermal resistances between layers, and (v) response to a thermal impulse. This complex set of conditions is common in many multilayer optoelectronic devices.

The calculated results are found to accurately compare with thermal measurements for OLEDs obtained using time-resolved infrared imaging under various operating conditions. The model predictions agree with the experimental data for two sets of electrophosphorescent OLEDs (or PHOLEDs), one emitting in green and the other in red.

This paper is organized as follows: In Sec. II, the transmission matrix approach along with some modifications that are specific to the PHOLED structure and thermal conditions is described. Section III details the experimental methods used for the assessment of thermal power dissipation and the measurement of the transient temperature response. The comparison between model prediction and experimental results are presented in Sec. IV and are analyzed in Sec. V. Also described in Sec. V is the application of these results to PHOLEDs to assess their potential for high intensity operation, including the use of substrates with a range of thermal conductivities, and under pulsed operation. We compare our results in this section with the more complex finite element method for solving differential equations, and find agreement between both approaches. In Sec. VI we present conclusions. The Appendix provides details of the calculation procedure.

II. THEORY

When a thin film with uniform thickness is subjected to an input heat flux, Q, incident on one surface, the one dimensional law of heat conduction, also known as Fourier's

a)Electronic mail: stevefor@umich.edu.

law, states that the heat flux is proportional to the negative of the local temperature gradient,

$$-\frac{\partial T(x,t)}{\partial x}=\frac{1}{K}Q(x,t), \tag{1a}$$

where $T(x,t)$ is the temperature of the thin film at point x and time, t, $Q(x,t)$ is the heat flux, and K is the thermal conductivity of the thin film. The continuity equation states that the heat flux at point x raises the temperature as follows:

$$\frac{\partial T(x,t)}{\partial t}=-\frac{1}{C}\frac{\partial Q(x,t)}{\partial x}, \tag{1b}$$

where $C=c_v\cdot\rho$ is the volumetric heat capacity, which is a product of specific heat at constant volume, c_v, and density, ρ. This equation expresses the conservation of heat in an infinitesimal thin film volume. Equations (1a) and (1b) are combined to yield

$$\frac{\partial T(x,t)}{\partial t}-\alpha\frac{\partial^2 T(x,t)}{\partial x^2}=0, \tag{2}$$

where $\alpha=K/(c_v\cdot\rho)$ is the heat diffusivity of the material. Internal heat generation is not included, and the solution is subject to the boundary conditions of both heat flux and temperature incident at the material surface.

Laplace transforms can be used to simplify the solutions to Eq. (1) yielding[9]

$$-\frac{\partial \hat{T}(x,s)}{\partial x}=\frac{1}{K}\hat{Q}(x,s), \tag{3a}$$

$$-\frac{\partial \hat{Q}(x,s)}{\partial x}=Cs\hat{T}(x,s), \tag{3b}$$

where $\hat{T}(x,s)$ and $\hat{Q}(x,s)$ are the Laplace transforms of the temperature and heat flux, respectively, and s is the Laplace variable. Pipes has shown that this system of equations has solutions expressed as follows:[8]

$$\begin{bmatrix}\hat{T}_1\\ \hat{Q}_1\end{bmatrix}=\begin{bmatrix}\cosh(\theta_i) & Z_i\sinh(\theta_i)\\ \dfrac{\sinh(\theta_i)}{Z_i} & \cosh(\theta_i)\end{bmatrix}\begin{bmatrix}\hat{T}_2\\ \hat{Q}_2\end{bmatrix}=\begin{bmatrix}A_i & B_i\\ C_i & D_i\end{bmatrix}\begin{bmatrix}\hat{T}_2\\ \hat{Q}_2\end{bmatrix}$$
$$=[T(\theta_i)]\begin{bmatrix}\hat{T}_2\\ \hat{Q}_2\end{bmatrix}, \tag{4}$$

where $\hat{T}_i(x,s),\hat{Q}_i(x,s)$ $(i=1,2)$ are the Laplace transforms of the temperature and heat flux on two sides of the layer of interest, i (1 is for the heat flux at the input, and 2 at the output), $\theta_i=L_i\sqrt{C_i s/K_i}$ is the operational propagation coefficient characterized by K_i, C_i, and L_i (the thickness of the ith layer), $Z_i=\sqrt{1/(K_iC_is)}$ is the characteristic thermal impedance of the layer, and A_i, B_i, C_i, and D_i $(D_i=A_i)$ denote the matrix elements.

Equation (4) represents a general approach to solve the transient thermal conduction problem for a multi-layer composite subject to boundary conditions as described by either the temperature or the heat flux at a given surface or interface. Since both the interface temperature and heat flux across interfaces between adjacent layers are continuous, the entire composite can be described as the product of matrices in series. An example representation of a two-layer composite, with layers denoted as i and j, is shown in Fig. 1(a).

To account for resistances to the thermal flux between layers, we consider the interface to be a thin layer with negligible specific heat. That is, letting $C_i=0$ in Eq. (4), we include interface effects with the reduced transmission matrix,

$$\begin{bmatrix}1 & R_{\text{int}}\\ 0 & 1\end{bmatrix}, \tag{5}$$

where R_{int} is the total (empirical) thermal resistance (m^2 K/W) of the interface.

The method can be further modified to incorporate radiation by introducing a parallel matrix describing power losses that additively combine, such as radiation and conduction. The parallel heat transfer pathway is shown schematically in Fig. 1(b), where $\hat{Q}^m_{1i}$ and $\hat{Q}^n_{1i}$ ($\hat{Q}^m_{2i}$ and $\hat{Q}^n_{1i}$) denote heat flux input (output) carried along two independent heat transfer pathways labeled m and n. In this case, m and n correspond to thermal conduction and radiation, respectively. Once again, following Pipes,[9] we therefore take into account both modes within a single layer of interest, i. Here $\hat{Q}^m_{1i}+\hat{Q}^n_{1i}$ is the Laplace transform of the total heat flux into i. Then, Eq. (4) can be rearranged as

$$\begin{bmatrix}\hat{Q}^k_{1i}\\ \hat{Q}^k_{2i}\end{bmatrix}=\begin{bmatrix}A^k_i/B^k_i & -1/B^k_i\\ 1/B^k_i & -A^k_i/B^k_i\end{bmatrix}\begin{bmatrix}\hat{T}_1\\ \hat{T}_2\end{bmatrix}, \tag{6a}$$

$$\begin{bmatrix}\hat{Q}_{1i}\\ \hat{Q}_{2i}\end{bmatrix}\equiv\sum_{k=m,n}\begin{bmatrix}\hat{Q}_{1i}\\ \hat{Q}_{2i}\end{bmatrix}=\sum_{k=m,n}\begin{bmatrix}A^k_i/B^k_i & -1/B^k_i\\ 1/B^k_i & -A^k_i/B^k_i\end{bmatrix}\begin{bmatrix}\hat{T}_1\\ \hat{T}_2\end{bmatrix}, \tag{6b}$$

where $k=m$ or n. Here, we assume the heat flux along the boundary plane between layers is negligible compared to the heat flux normal to the layers.

In a typical OLED, the heat source is assumed to be the emission layer (EML) combined with the hole transport layer (HTL), the electron transport layer (ETL), and the exciton

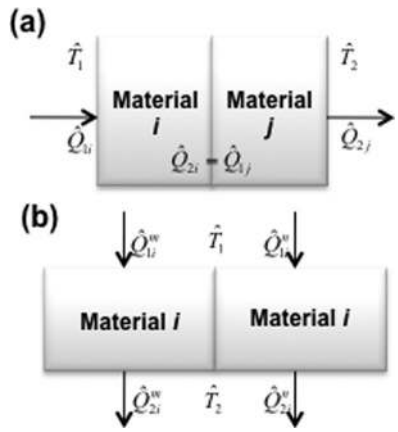

FIG. 1. (a) Heat flow for layers in series. Here, T_1 and T_2 denote the Laplace transformation of ambient temperatures on both sides of the composite; $\hat{Q}_{2i(j)}$ and $\hat{Q}_{1i(j)}$ are the thermal input and outflow of material $i(j)$. Here, $\hat{Q}_{2i}=\hat{Q}_{1j}$ is based on the continuity of the interface heat flux between adjacent layers. (b) Heat flow for layers in parallel, where $\hat{Q}^m_{1i}$, $\hat{Q}^n_{1i}$ denote input heat flux carried by two thermal dissipation modes, and $\hat{Q}^m_{1i}+\hat{Q}^n_{1i}$ is the total heat flux into material, i.

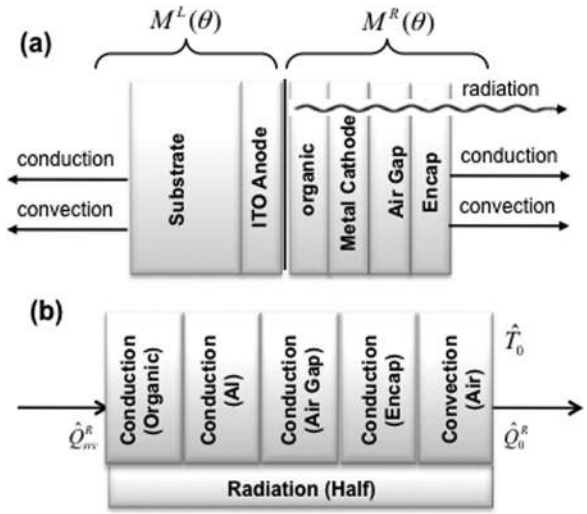

FIG. 2. (a) Illustration of the series and parallel heat pathways for an OLED used in setting up the matrix product. The matrix product describing the thermal flux to the left is $M^L(\theta)$, and is composed of transport in air, glass substrate, and ITO anode in sequence, and $M^R(\theta)$ is the product for thermal transport to the right, composed of the organic layer, metal cathode, air gap, encapsulation, and air in sequence. (b) The construction of $M^R(\theta)$, where $\hat{T}_{src}$ and $\hat{T}_0$ are the source and ambient temperatures, respectively, $\hat{Q}^L_{src}$ and $\hat{Q}^R_{src}$ are the heat fluxes dissipated through the left and right surfaces, and $\hat{Q}^L_{src}+\hat{Q}^R_{src}$ is the total thermal power flow. The conduction matrices for the organic, metal cathode, and air layers are multiplied in sequence while radiation is incorporated as a parallel pathway.

blocking layer (EBL), embedded inside the multilayer composite, as shown schematically in Fig. 2(a). That is, we need to consider the case where the layers themselves act as heat sources, rather than simply as heat-transfer media. Since the thermal properties of these various organic thin films are often similar, for simplicity and without loss of generality we assume only a single organic layer characterized by the average thermal constants of all such layers comprising the OLED active region. As shown in Fig. 2(a), we characterize this feature by analyzing two sub-matrices, $M^L(\theta)$ and $M^R(\theta)$, one to the left and the other to the right of the heat source, respectively. We then separate the heat flux input into two parts, Q^L_{src} and Q^R_{src}, following the boundary condition:

$$Q^L_{src}+Q^R_{src}=Q_{therm}=JV-Q_{opt}, \tag{7}$$

where Q^L_{src} and Q^R_{src} are the heat fluxes input to the left and right matrices, respectively, Q_{therm} is the thermal power generation of the device, J and V are the current density and voltage required for device operation, and Q_{opt} is the power removed in the form of emitted light. Thus, Eq. (4) becomes

$$\begin{bmatrix}\hat{T}_{src}\\ \hat{Q}^{L,R}_{src}\end{bmatrix}=\left[M^{L,R}(\theta)\right]\begin{bmatrix}\hat{T}_0\\ \hat{Q}^{L,R}_0\end{bmatrix}, \tag{8}$$

where $\hat{T}_{src}$ and $\hat{T}_0$ are Laplace transforms of the source and ambient temperatures, respectively, and Q^L_{src} and Q^R_{src} are the Laplace transforms of heat fluxes dissipated through $M^L(\theta)$ and $M^R(\theta)$, respectively. In this study, $M^L(\theta)$ is composed of the conduction matrices for the indium tin oxide (ITO) anode, glass substrate, and air in sequence, and $M^R(\theta)$ is composed of the thermal conduction matrices for a single composite organic layer, metal cathode, and air in sequence, as shown in Fig. 2(b). For devices with encapsulation, the matrices for the air gap $\left[T(\theta_{AirGap})\right]$ and the glass lid $\left[T(\theta_{Encap})\right]$ have to be included in the matrix product.

For radiative losses, we use the Stefan-Boltzmann law,

$$\begin{aligned}Q_{rad}&=\varepsilon\sigma(T^4_{src}-T^4_0)=\varepsilon\sigma(T^2_{src}+T^2_0)(T_{src}+T_0)(T_{src}-T_0)\\&\cong h_{rad}(T_{src}-T_0),\end{aligned} \tag{9}$$

where the last term on the right is an approximation for $T_{src}\approx T_0=300$ K, which is the ambient temperature. Here, ε is the emissivity of the OLED gray body (assumed to equal 0.5 for this study[3]), and σ is the Stefan-Boltzmann constant. Now, we have $h_{rad}\approx 5\ \mathrm{W/m^2\ K}$ for an estimated 20 °C temperature rise. The linear radiation approximation is treated as a parallel matrix following Eq. (5),

$$\begin{bmatrix}1 & R_{rad}\\ 0 & 1\end{bmatrix}, \tag{10}$$

where $R_{rad}=1/h_{rad}$ is the thermal resistance to radiation (in the case of radiation, the heat capacity is zero). Combining Eqs. (4) and (10) into Eq. (6b), we obtain the total matrix, $M^R(\theta)$, that takes into account conduction, convection, and radiation,

$$\left[M^R(\theta)\right]=\begin{bmatrix}A^R & B^R(1-\gamma_{rad})\\ C^R(1+\gamma_{rad}) & A^R\end{bmatrix}, \tag{11}$$

where $\gamma_{rad}=B^R/R_{rad}\ll 1$ is the radiation perturbation term, and A^R, B^R, and C^R are the matrix elements of the product of 2×2 matrices: $[T(\theta_{Org})][T(\theta_{Al})][T(\theta_{AirGap})][T(\theta_{EnCap})][T(\theta_{Air})]$. The left matrix, $M^L(\theta)$, can be similarly constructed. Convection in this case is treated analogously to conduction, where an effective conductance, K_{conv}, is used to characterize the heat removal at the boundary between the OLED surface and the ambient. Here, K_{conv} depends on the ambient conditions, significantly varying between cases such as stagnant or forced-air cooling.

III. EXPERIMENT

We studied two sets of PHOLEDs of different sizes: 1 mm × 1 mm unencapsulated fac-*tris*(phenylpyridine) iridium ($Ir(ppy)_3$) devices on 1 cm × 1 cm substrates, and 5 cm × 5 cm large-area encapsulated devices (provided by Universal Display Corp., Ewing, NJ). The small devices were used to investigate two-dimensional (2-D) heat spreading, whereas the larger devices allowed for a direct comparison of the experiment to our 1-D model. Note that for lighting applications, the devices are expected to be large (i.e., they occupy a significant fraction of the substrate area), and hence the 1-D approach is more suitable, whereas small devices approximate point heat sources in such applications as intense light emitters (e.g., lasers).

The 1 mm^2 devices were prepared as follows. A 20 Ω/sq, pre-patterned (in 1 mm stripes) ITO-coated glass substrate was degreased in detergent solution, followed by thorough rinsing in de-ionized water. The substrate was then boiled in

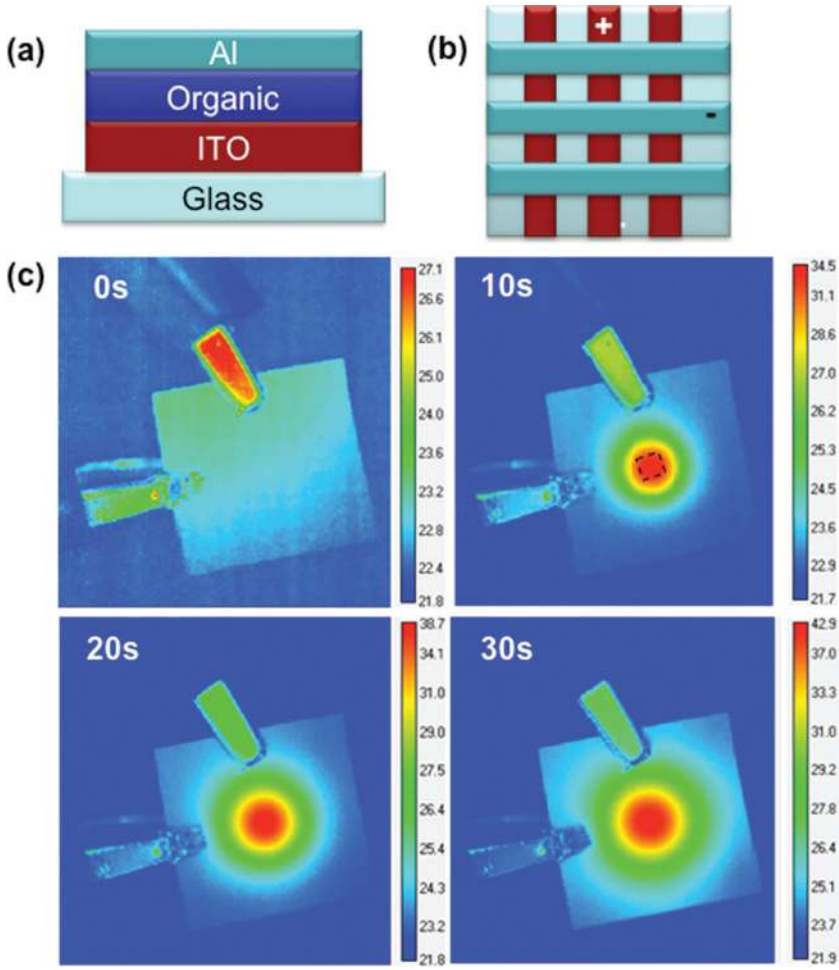

FIG. 3. (Color) (a) Schematic structure of small-area $Ir(ppy)_3$ devices: glass (1 mm)/ITO (120 nm)/organic layers (105 nm)/Al cathode (100 nm). (b) Patterning of the ITO and Al anode and cathode stripes, each 1 mm wide. (c) Thermal images of the $Ir(ppy)_3$ device under a fixed voltage of 10 V (corresponding to a current density of 1 A/cm^2) after 10, 20, and 30 s operation following the onset of the voltage ramp. The dashed square indicates the device location.

trichloroethane, and rinsed in acetone in an ultrasonic tank, boiled in isopropanol, and dried in pure nitrogen gas. Next, the substrate was exposed to UV/ozone for 10 min prior to transfer into a high vacuum ($\sim 10^{-7}$ Torr) deposition chamber. A 40 nm-thick HTL consisting of 4,4′-bis[N-(1-naphthyl)-N-phenyl-amino]-biphenyl was followed by a 25 nm-thick $Ir(ppy)_3$ doped at 8 wt. % in a 25 nm-thick 4,4′-bis(N-carbazolyl)biphenyl host as the phosphorescent emission layer (EML); a 40 nm-thick 2,9-dimethyl-4,7-diphenyl-1,10-phenanthroline (BCB) layer was used as the combined ETL and EBL followed by a 10 nm-thick Li doped BCP layer in a 1:1 molar ratio, and finally capped with a 100 nm-thick Al cathode. Undoped BCP was used to prevent Li diffusion into the EML, and to maintain the charge balance at high bias. The 1 mm^2 device structure and the electrode pattern designs for the large and small devices are shown in Figs. 3(a) and 3(b).

The large-area green and red PHOLEDs emit at peak wavelengths of $\lambda = 530$ nm and 630 nm, respectively. The structure of these two packaged devices is as follows: glass (0.7 mm)/ITO (120 nm)/organic layers (120 nm)/Al cathode (100 nm)/air gap (30 μm)/glass encapsulation (0.7 mm) (see Fig. 4(a)). Encapsulation prevents degradation of the devices due to contact with air or moisture over the extended testing sequence. Figure 4(b) shows the 5 cm $\times$ 5 cm ITO and Al patterns on the glass substrate. It is important to provide uniform current injection to achieve homogeneous emission across the entire device area. The sheet resistivity of the ITO anode (20 Ω/sq) is considerably greater than that of the Al cathode (0.3 Ω/sq for 100 nm thick Al),[10,11] making uniform current injection from the anode particularly challenging. Hence, both the anode and cathode are pumped from two opposing contacts, as shown in Fig. 4(b). Here, hole injection is via the top and bottom contacts in the figure, and electron injection is from the left and right contact pads.

The J-V characteristics of the completed devices were measured using a semiconductor parameter analyzer (HP 4145B). Optical characterization of the devices employed a calibrated reference detector using standard methods.[12] The fraction of the total input power flux removed through non-dissipative optical emission (Q_{opt}) was calculated based on output spectra and luminance at a fixed current density, i.e., $Q_{opt} = 1.7[I_{ph}/R_{\lambda}A]$. Here, I_{ph} is the detector photocurrent corresponding to light output in the forward-viewing direction, R_{λ} is its wavelength-weighted-average responsivity over the PHOLED spectrum, and A is the PHOLED emitting area. The factor 1.7 adjusts for non-absorbed light emitted in all directions, including waveguide and glass-mode emission.[13] Thermal surface image measurements were acquired using a non-contact thermal camera (FLIR A325). To eliminate stray light and to provide a thermally stable environment where the images were taken, samples were inserted into a box with a light absorbing black interior. The PHOLED current was provided via a Keithley 2400 source meter.

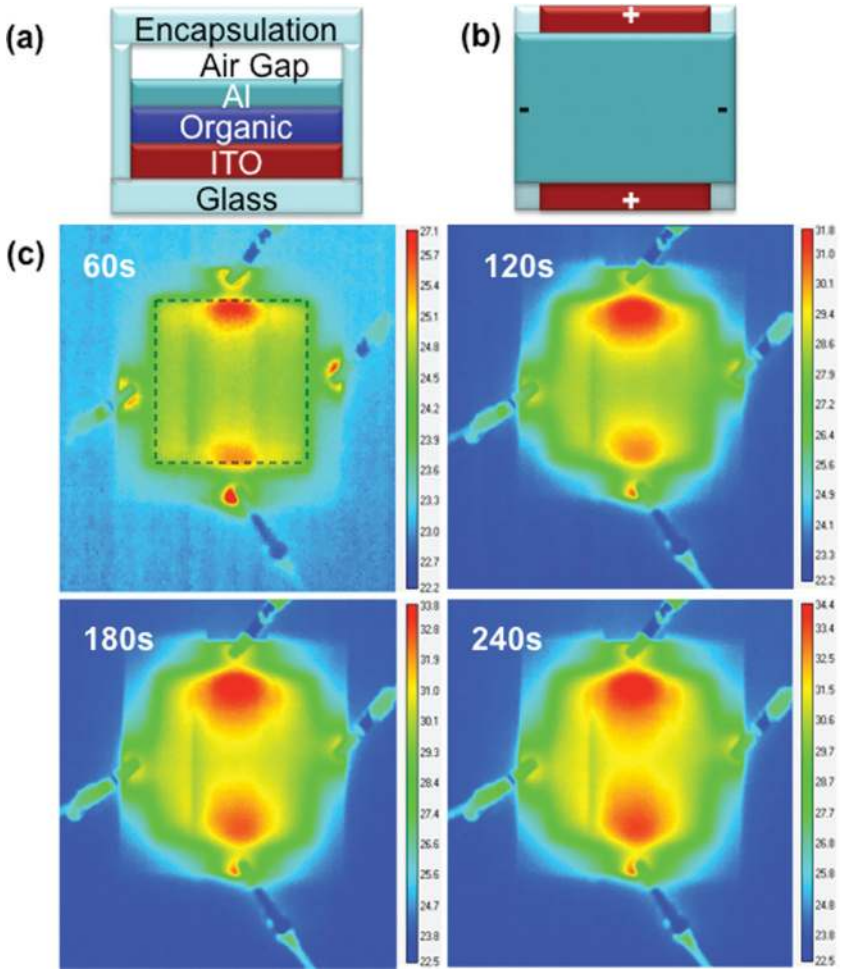

FIG. 4. (Color) (a) Schematic structure of large-area devices: glass (0.7 mm)/indium tin oxide (120 nm)/organic layers (120 nm)/Al cathode (100 nm)/air gap (30 μm)/glass encapsulation (0.7 mm). (b) Illustration of the patterns used for the ITO and Al anode and cathode contacts, both 5 cm wide. (c) Thermal images of the large-area green device under a fixed voltage of 7 V (or a current density of 3.4 mA/cm^2) after 60, 120, 180, and 240 s operation following the onset of the voltage ramp. The dashed square indicates the device location.

The transient temperature data for each sample were obtained by tracking their thermal images under various current densities. For this purpose, the frame rate of the thermal imaging system was 60 Hz, which is adequate for the purposes of these experiments. Two sets of data were recorded: device heat-up and cool-down. To capture the transient temperature rise, the devices were operated under constant voltage for 5 min until equilibrium was reached, with their thermal images captured at a frame rate of 2 s^{-1}. To observe the cool-down dynamics, the devices were turned off after reaching equilibrium at a fixed V, and the temperature transient was similarly obtained until room temperature was reached.

IV. RESULTS

Figure 3(c) shows the surface thermal images (as viewed from the substrate) of the 1 mm^2 Ir(ppy)$_3$ device after 10, 20, and 30 s following the onset of a 10 V step (corresponding to $J = 1$ A/cm^2). While the thermal distribution is localized around the light-emitting area, it is observed to spread out from the active device region. The temperature difference between the center of the device and the substrate edges after 60 s is 21 °C after equilibrium is established following the onset of the current step (Fig. 3(c)).

To model the relationship of temperature versus thermal flux, a uniformly distributed, well-defined temperature profile is needed. For this purpose, we use the large-area devices. Figure 4(c) shows the transient thermal images (also measured from the substrate surface) of the large-area green device at 7 V (corresponding to $J = 9$ mA/cm^2) after 60, 120, 180, and 240 s following the onset of the voltage step. There is a pronounced temperature variation across the device area, with higher temperatures close to the anode contacts near the device edge. This results from the high ITO resistivity that provides less current near the device center than at its edges. The temperature variation across the surface is within 1.8 °C when the devices are operated at 5.5 V $< V <$ 7.0 V, corresponding to peak surface temperatures from 24 to 36 °C. The temperatures reported here are medians in the range detected by the thermal camera over the active device area, thereby ignoring the minor thermal gradients observed.

The external quantum efficiency (*EQE*) and *PE* for the large-area green and red emitting PHOLEDs are shown in Figs. 5(a) and 5(b), respectively. The corresponding *J-V* characteristics are shown in Fig. 6, along with the luminance-current density (*L-J*) characteristics. The estimated heat flux contributions under each operating condition are summarized for the large-area green device in Table I, and for the red PHOLED in Table II.

Now, the total input power flux is $Q_{tot} = J \cdot V$. The thermal power dissipation is then given by $Q_{therm} = Q_{tot} - Q_{opt}$. For the green device at a luminance of between 540 and 620 cd/m^2 and the analogous red device at a luminance of between 220 and 240 cd/m^2, approximately 97 to 99% of the

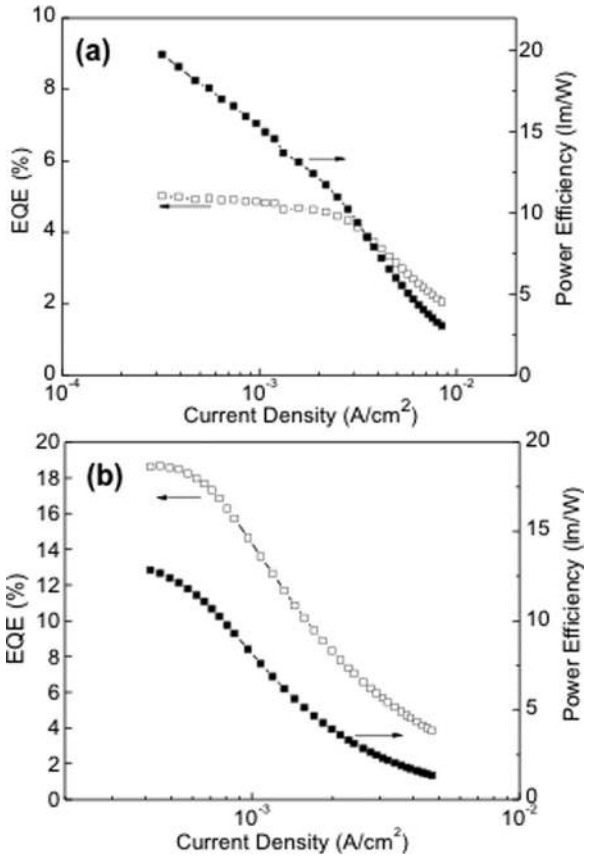

FIG. 5. The external quantum (*EQE*) and power efficiencies (*PE*) vs the drive current density of large-area (a) green, and (b) red electrophosphorescent OLEDs (PHOLEDs).

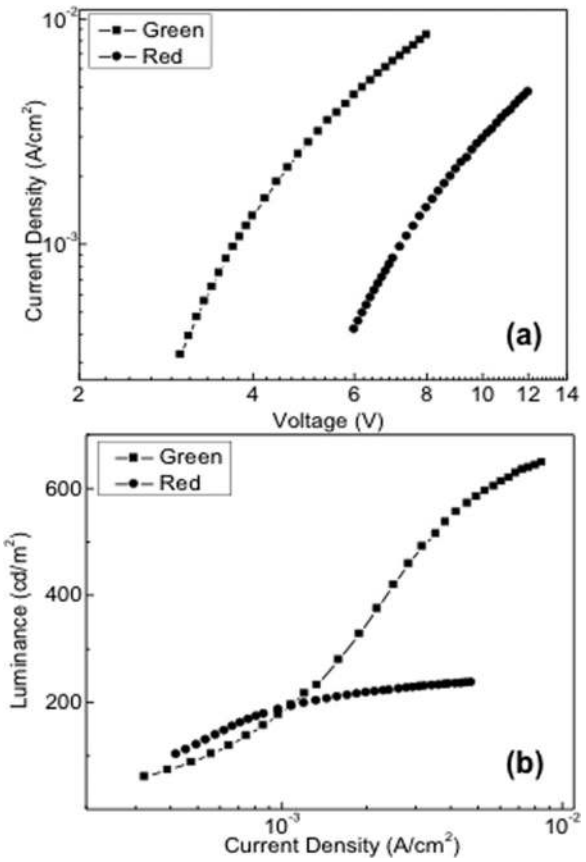

FIG. 6. (a) Current density vs voltage (*J-V*), and (b) luminance vs current density (*L-J*) characteristics of large-area green (squares) and red (dots) PHOLEDs.

total power is dissipated through several thermal channels including conduction, convection, and radiation (see calculated values based on measured device efficiencies for Q_{therm}/Q_{tot} listed in Tables I and II).

Figure 7 shows the device surface temperature at various V for the large-area green and red PHOLEDs following the onset of the voltage step (symbols). These results are compared with the matrix model calculations indicated by the solid lines. For the green device (Fig. 7(a)), the temperature was obtained at 5.5, 6.0, 6.5, and 7.0 V, corresponding to $Q_{therm} = 197$, 270, 353, and 447 W/m^2, respectively. The data for the red device are similarly shown in Fig. 7(b) at 9.0, 10.0, 11.0, and 12.0 V, corresponding to $Q_{therm} = 188$, 288, 413, and 563 W/m^2, respectively.

To compare the temperature of the heat-generating layer (i.e., the EML at temperature, T_{src}) to the device surface temperature (corresponding to the calculations and measurements in Fig. 7, respectively), we calculate the thermal gradient across the device. The resulting gradient obtained using Eq. (1a) is shown in Fig. 8 for the ITO and glass substrate, assuming thermal fluxes, $Q_1 = 197$, $Q_2 = 270$, $Q_3 = 353$, and $Q_4 = 447$ W/m^2 for the green device under the same conditions of operation as in Fig. 7 and Table I. For all of the power densities considered, a temperature difference of approximately 0.1 °C is observed between the source layer and the substrate surface. Since the measured surface temperature is 30 °C, this small difference contributes a negligible error to our fits in Fig. 7. Note that the thermal gradient from the EML to the top package surface is expected to be larger due to the presence of the metal cathode, air gap, and glass encapsulation layer (cf., Fig. 2).

Figure 9 shows the surface temperature under various voltages following the end of the voltage pulse (data points), in which case the device cools to the ambient temperature of

TABLE I. Summary of efficiency and thermal parameters of the large-area green PHOLED.

Voltage (V)	Current density (mA/cm^2)	Q_{tot} (W/m^2)	Q_{opt} (W/m^2)	Q_{therm}/Q_{tot} (%)
5.5	3.69	203	6	97
6.0	4.60	276	6	98
6.5	5.52	359	6	98
7.0	6.48	454	7	98

TABLE II. Summary of efficiency and thermal parameters of the large-area red PHOLED.

Voltage (V)	Current density (mA/cm^2)	Q_{tot} (W/m^2)	Q_{opt} (W/m^2)	Q_{therm}/Q_{tot} (%)
9	2.15	194	6	97
10	2.94	294	6	98
11	3.81	419	6	99
12	4.74	569	6	99

$T \cong 25\,^{\circ}\mathrm{C}$. As in Fig. 7, the results are similarly compared with transmission matrix model calculations (solid lines).

V. DISCUSSION

The results of the thermal power calculations in Sec. II under selected drive conditions are provided in Tables I and II. The thermal transients are shown in Fig. 7, in both cases using the materials thermal properties summarized in Table III. The temperatures are found by inverting the matrix in Eq. (6), given the thermal input vector, $\hat{Q}$. This is accomplished through a polynomial expansion whose order is determined by meeting the convergence criterion, as discussed in the Appendix. We find that a 4th order polynomial results in an error of only $\pm 2\%$ compared to higher order solutions, and hence is used for all results discussed here.

From Fig. 7, the maximum temperature increase for the green PHOLED is 10 °C at 7.0 V (corresponding to $J = 6.48$ mA/cm^2, or $Q_{tot} = 454$ W/m^2), and 11.5 °C for the somewhat less efficient red device at 12.0 V (corresponding to $J = 4.74$ mA/cm^2, or $Q_{tot} = 569$ W/m^2). There are no adjustable parameters used in the calculation with the exception of those

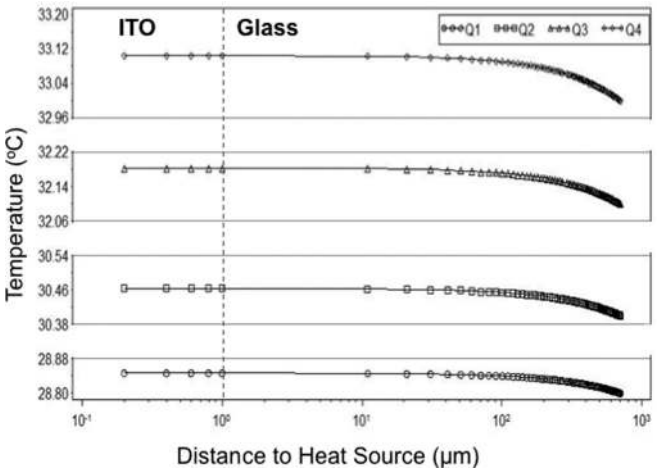

FIG. 8. Calculated temperature gradient across the ITO and glass layers for heat fluxes of $Q_1 = 197$ W/m^2, $Q_2 = 270$ W/m^2, $Q_3 = 353$ W/m^2, and $Q_4 = 447$ W/m^2 generated in the PHOLED light emitting layer (EML). The surface temperatures at each heat flux are obtained from measurements using infrared imaging. The small thermal gradient suggests that the thermal measurements made at the glass surface are an accurate determination of the temperature of the EML.

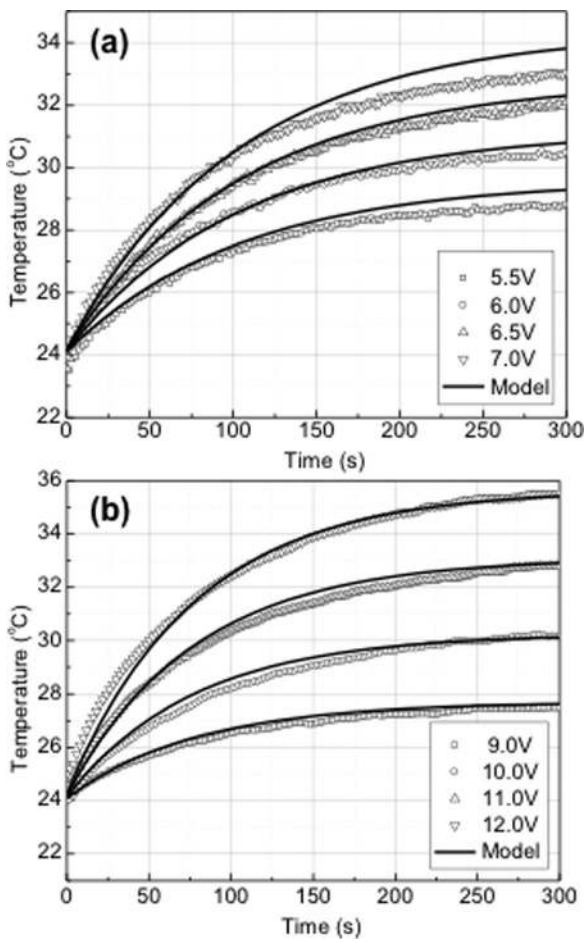

FIG. 7. Transient temperature response (open symbols) measured using infrared imaging at different voltages for large-area (a) green, and (b) red PHOLEDs following the onset of the voltage step. The results are compared with transmission matrix model calculations (solid lines). The corresponding drive currents and other operating parameters for these conditions are provided in Tables I and II, with the parameters used for the calculations provided in Table III.

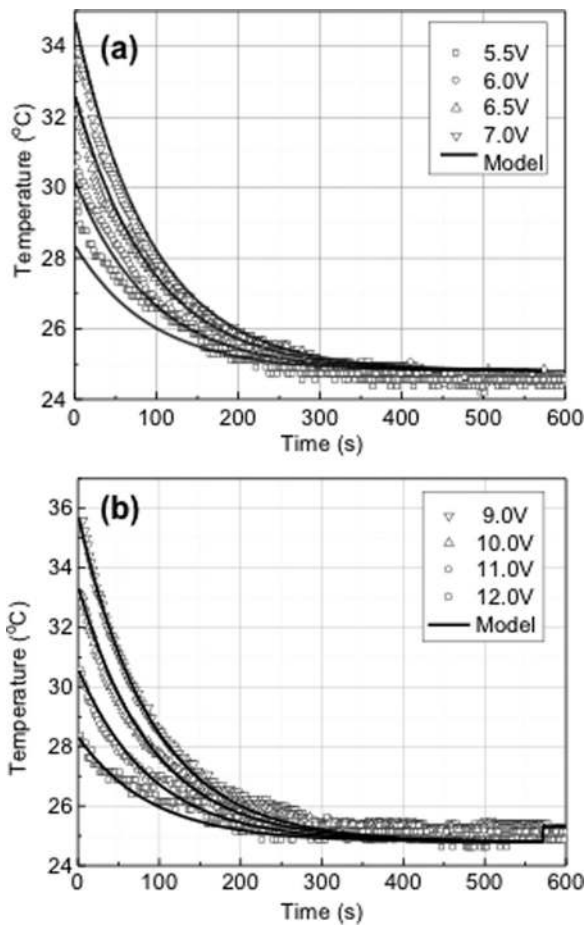

FIG. 9. Transient temperature response (open symbols) measured using infrared imaging at different voltages for large-area (a) green, and (b) red PHOLEDs following the end of the drive voltage step at time, $t = 0$. The devices were operated at a fixed voltage until temperature equilibrium was reached. The results are compared with transmission matrix model calculations (solid lines). The corresponding drive currents and other operating parameters for these conditions are provided in Tables I and II, with the parameters used for the calculations provided in Table III.

TABLE III. Summary of the thermal parameters used in modeling.

Materials	Thickness (μm)	Density (kg/m^3)	Heat capacity (J/kgK)	Thermal conductivity (W/Km)	Reference
Air	…	1.2	1.0×10^3	2.5×10^{-2}	15, 16
Glass	700	2.6×10^3	8.2×10^2	3.0	23
ITO	1	7.2×10^3	3.4×10^2	8.0	24
Organic	0.1	1.2×10^3	1.7×10^3	2.0×10^{-1}	25
Al	0.1	3.9×10^3	9.0×10^2	2.0×10^1	26, 27
Air gap	30	1.2	1.0×10^3	2.5×10^{-2}	15, 16
Encap	700	2.6×10^3	8.2×10^2	3.0	23

used to model convective losses, i.e., the thermal conductivity and the thickness of the air boundary layer and the radiative emissivity, as we will discuss next. There are only small discrepancies between the model prediction and the experimental results. The largest disagreement is for the green device at 7.0 V, where the steady-state calculated temperature is 0.9 °C higher than observed. This difference is possibly due to uncertainties in measuring device temperature arising from thermal inhomogeneities introduced by the resistive ITO contact apparent in Fig. 4(c).

An advantage of the matrix methodology is the simplification of the calculation of the thermal transient response. For example, the response of the devices following the current pulse is modeled by introducing the Laplace transform of a step function into the heat source term. In this case, we define the thermal input function, $f(t)$, as

$$f(t) = \begin{cases} 0, -\infty < t < -t_0 \\ Q, -t_0 \le t < 0 \\ 0, 0 \le t < +\infty \end{cases}, \tag{12}$$

where t is time, and t_0 is the duration of a constant heat flux pulse, Q. The corresponding Laplace transform is

$$\begin{aligned} L\{f(t)\} &= Q \cdot L\{u(t+t_0)\} - Q \cdot L\{u(t)\} \\ &= Q \cdot \left(\frac{e^{t_0 s}}{s} - \frac{1}{s}\right) = Q \cdot \sum_{k=1}^{+\infty} \frac{(t_0 s)^k}{s \cdot k!}, \end{aligned} \tag{13}$$

where $u(t)$ is the unit step function. Figure 9 shows the thermal transient response at $t_0 = 120$ s as measured for the green (Fig. 9(a)) and red (Fig. 9(b)) PHOLEDs using time-resolved thermal imaging (data points) compared to the transmission matrix model calculations. The measurement and the calculated heat response are in reasonable agreement for the duration of the cooling transient under the same bias conditions as employed in Fig. 7, where we modeled the device turn-on transients.

To obtain the fits in Figs. 7 and 9, both radiation and convection are included in the matrices that describe the composite thermal system. Indeed, R_{rad} and t_{air} are two fitting parameters in this study, where the equilibrium temperature is sensitive to t_{air}, and the thermal transient response is somewhat sensitive to our choice of R_{rad}. The fits yield the radiative resistance, which is a parallel heat loss channel to both conduction and convection, giving $R_{rad} \approx 0.2$ m^2 K/W for the green device, and $R_{rad} \approx 0.4$ m^2 K/W for the red device, which agree with the ideal gray-body estimate of $1/R_{rad} = h_{rad} \approx 5$ W/m^2 K in Sec. II. The higher thermal resistance of the red PHOLED is consistent with its lower efficiency (with $PE = 4.3$ to 7.8 lm/W for green versus 1.3 to 3.6 lm/W for red; see Tables I and II). Table III summarizes the thermal parameters used for modeling the structure in Fig. 4(a), e.g., layer thickness, material density, heat capacity, and thermal conductivity.[23–27]

Developing an accurate model for convection depends on the ambient conditions (e.g., forced air versus a stagnant, or free, air layer, and whether a heat sink is employed, etc.). In our case, we assume free convection,[14] where the thermal boundary between the device radiating surface and the ambient is modeled by an effective thermal conductivity, k_{air}, and boundary layer thickness, t_{air}. To approximate these parameters for the PHOLEDs used here, we simulated the thermal conditions by positioning a thermometer at different distances from a "semi-infinite" hot surface (i.e., a hot plate) maintained at 30 to 40 °C. In contrast to radiation which only depends on the temperature and emissivity of the surface, convection depends on the orientation of the hot surface, e.g., whether it is horizontal or vertical. In our case, the hot plate was vertically positioned to be consistent with the PHOLED orientation, although the orientation was not found to significantly affect our measurements over the temperature range studied. By measuring temperature versus distance, we obtain $t_{air} = 1$ to 5 cm. For matrix fitting under the conditions listed in Table I and II, we assume $t_{air} = 1.1$ cm is obtained for the green device, and $t_{air} = 1.2$ cm for the somewhat hotter red PHOLED for these fits. In addition, $k_{air} = 0.025$ W/K m (see Table III) was obtained from Refs. 15 and 16.

Although we have measured the specific convection conditions that apply in our experiments, the sensitivity of the calculations to k_{air} is a potentially significant source of error. This is apparent from the plot in Fig. 10, where the device temperature is calculated as a function of $0.01 < k_{air} < 0.20$ W/K m for a constant thermal flux input of 100, 200, 500, and 1000 W/m^2 and an ambient temperature of 25 °C. A sensitive dependence on the air conductivity is observed over the range of $0.01 < k_{air} < 0.05$ W/K m. Since the fitted value of $k_{air} = 0.025$ W/K m is typical of free convection, this result suggests that to avoid unacceptable thermal increases at very high PHOLED operating powers, forced air convection is required.

Finally, we consider the effects of thermal contact resistances, R_{int}, between the various interfaces. Its incorporation is analytically straightforward by the inclusion of interface

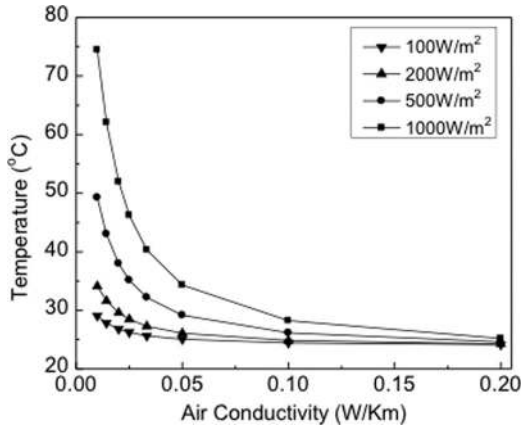

FIG. 10. Calculated PHOLED temperature due to convective losses as a function of air conductivity at input heat fluxes of 100, 200, 500, and 1000 W/m^2.

matrices in the series product in Eq. (5). Note, however, that the accurate measurement of R_{int} in complex composite systems such as PHOLEDs and other multilayer devices can be problematic. For the devices shown in Fig. 4, the most resistive interfaces are at the boundaries between ITO and the organic composite, and between the organics and the Al cathode. It has been shown[17] that for these systems, $R_{int} = 1 \times 10^{-8}$ m^2 K/W. Although a nonlinear dependence of the interface resistances on temperature has also been reported,[18] such effects have been neglected for simplicity.

Given that the model introduced in Sec. II is both straightforward to implement and is accurate for a well-defined set of thermal parameters, it is useful to extend it to PHOLEDs operating under a range of practical conditions. For example, we have applied this model to explore the effects of substrates with a variety of thermal conductivities. These include glass, sapphire ($K = 35$ W/K m) and Si ($K = 150$ W/K m), as shown in Fig. 11. Compared to glass substrates, the device temperature rise is considerably smaller for a thermal power input > 1 kW/m^2. For example, at $Q_{therm} = 5$ kW/m^2, the temperature rise is only 1.3 °C for Si, 9.8 °C for sapphire, and 82 °C for glass.

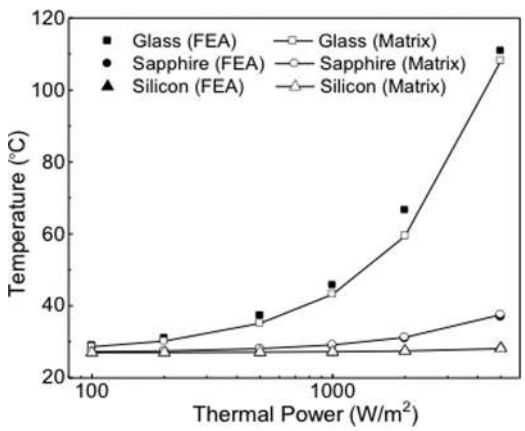

FIG. 11. Calculated PHOLED temperature (open dots) as a function of thermal input power for devices using glass, sapphire, and silicon substrates. The results are compared with the finite element analysis (solid dots). Where only matrix results are shown (open symbols), the differences with FEA calculations are negligible on the scale of the plot.

For comparison, the corresponding results obtained using conventional finite element analysis (FEA) to solve the system of partial differential equations describing the multilayer PHOLEDs are also shown in Fig. 11. For the FEA calculation, we use the Comsol Multiphysics solver as a test of our matrix-based approach. The systematically higher temperature obtained from FEA above 40 °C is possibly due to the 2-D geometry assumed, where a device area of 1 mm $\times$ 1 mm is employed to accommodate the grid for the ultra-thin film structure. Compared to the FEA, the matrix calculation is far less computationally intensive for calculating temperature profiles of large-area devices since it simplifies the complex and time consuming calculations needed for arbitrary multi-layer structures. Furthermore, the physical parameters are easily identified, and their corresponding effects on the total thermal dissipation can be efficiently analyzed. Ultimately, the matrix model allows for the rapid iteration of both structure and materials properties that can be used to optimize thermal management in complex structures. This capability has proven invaluable in the design of the optical properties of multilayer structures using an analogous optical matrix approach.[19]

A second application is to estimate the temperature increase under very high current pulses required for high intensity illumination or even electrically driven organic lasers.[20] Figure 12 shows the thermal response following 1, 5, and 10 ms pulses for an ultrahigh thermal flux of 10^6 W/m^2. For each case, the thermal parameters and device structures are the same as those for the large-area devices. Here, $R_{rad} \approx 0.4$ m^2 K/W is used, similar to that of the large-area red device. Also, for these calculations, we assume $t_{air} = 5$ mm compared to that used under a lower power, steady-state operation of the large-area devices (where we measure $t_{air} = 1.1$ to 1.2 cm). In this case, we assume that an equilibrium air boundary does not fully develop during the very short heat pulse.

While the thermal response is somewhat sensitive to the choice of t_{air}, we observe a nearly logarithmic decay in

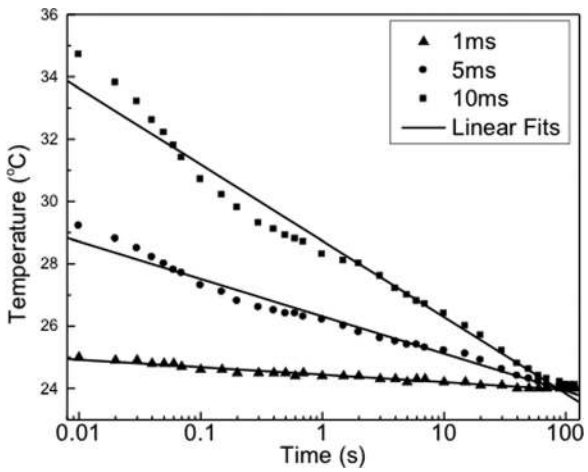

FIG. 12. Temporal response of the PHOLED temperature (solid dots) at various pulse widths of 1, 5, and 10 ms under a fixed, ultrahigh thermal input power of 10^6 W/m^2. Linear fits are displayed as solid lines. The physical and thermal parameters are the same as for the large-area devices. Now, $R_{rad} \approx 0.4$ m^2 K/W, whereas $t_{air} \approx 5$ mm is used here compared to that of the large-area devices due to the short pulse duration.

temperature, as shown by the solid lines in Fig. 12; maximum temperatures of 25.0, 28.9, and 33.9 °C for pulse durations of 1, 5, and 10 ms, respectively. Clearly, the effects of convection under both steady-state and pulsed operation are complex, and are beyond the scope of this study. Hence, further study of these effects is required to fully understand thermal transients under very high device excitation.

VI. CONCLUSIONS

In this work, we use a transmission matrix formalism to accurately model the thermal response of multilayer composite structures typical of OLEDs and other optoelectronic devices. The model, based on Laplace transforms, is used to determine the steady-state and transient thermal response of multilayer PHOLEDs used in display and lighting applications. The model results are compared with measurements of encapsulated large-area PHOLEDs obtained via thermal imaging. The formalism is used to account for diverse series and parallel power loss channels including conduction, convection, light emission, and thermal radiation. Agreement is obtained between the model and observation using only measured properties such as thermal conduction, interface thermal resistance, and convective boundary layers, thereby validating the approach.

The results offer insights for the temperature management of organic electronic devices, and, in particular, of OLEDs employed at high intensity, as required for lighting applications. For example, forced convection can lead to doubling of the effective air conductivity, thereby lowering the device temperature at high drive currents. The model, which is similar to transmission matrix formalisms used to calculate optical fields in multilayer composites, can be adapted to the study of a variety of thermal conditions and device structures, making this work a significant advance in understanding and controlling the temperature response of a range of important optoelectronic devices.

ACKNOWLEDGMENTS

The authors thank Mr. Kevin Bergmann for helpful discussions. We are grateful to the U.S. Department of Energy, Energy Frontier Center at the University of Southern California (Award No. DE-SC0001011, XQ, experiment, analysis) and the Universal Display Corp. (SRF, analysis) for financial support of this work. We also thank a Small Business Innovation Research program subcontract funded by the U.S. Department of Energy through the Universal Display Corporation (SRF, experimental methods) for partial financial support.

APPENDIX: INVERSE LAPLACE TRANSFORM CALCULATION

The numerical system stability is important for obtaining an accurate calculation of the inverse Laplace transform. Here, the matrix elements in Eq. (4) are calculated using a series expansion of the form,[21]

$$A_i = D_i = \cosh\left(L_i\sqrt{s/a_i}\right) = \sum_{k=0}^{\infty}\frac{L_i^{2k}}{(2k)!a_i^k}s^k, \qquad \text{(A1)}$$

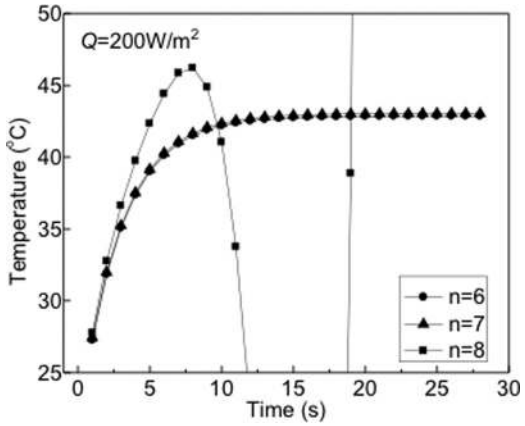

FIG. 13. Heat transfer for the multilayer composite PHOLED is calculated using different polynomial expansion orders ($n=6$, 7, and 8). Note the convergence of the solutions for $n=6$ and $n=7$, whereas the solution becomes unstable at $n=8$.

$$B_i = R_i = \sinh\left(L_i\sqrt{s/a_i}\right)\Big/\left(L_i\sqrt{s/a_i}\right) = R_i\sum_{k=0}^{\infty}\frac{L_i^{2k}}{(2k+1)!a_i^k}s^k, \qquad \text{(A2)}$$

$$C_i = L_i\sqrt{s/a_i}\sinh\left(L_i\sqrt{s/a_i}\right)\Big/R_i = \frac{1}{R_i}\sum_{k=1}^{\infty}\frac{L_i^{2k}}{(2k-1)!a_i^k}s^k, \qquad \text{(A3)}$$

where s is the Laplace variable, and A_i, B_i, and C_i are the matrix elements of the ith layer, as defined in Eq. (4). Additionally, L_i, R_i, and a_i are the thickness, thermal resistance, and thermal diffusivity of the ith layer, respectively.

The convergence of these polynomial expansions must be tested for convergence to be rigorously valid and free from large errors. A convergence problem originates from the instability of the inverse Laplace transformation function obtained from the power series in Eqs. (A1)–(A3).[22] As shown in Fig. 13, the temperature rise for a model, 1-mm-thick glass slab where $Q_{therm}=200$ W/m^2 is calculated for various polynomial orders ($n=6$, 7, and 8), with the roots of the truncated polynomial provided in Table IV. A stable solution requires that all poles have a negative real part in the case of $n=6$ and 7. For $n=8$, two roots have a positive real

TABLE IV. Roots of the truncated denominator polynomial.

	Polynomial order		
Root	$n=6$	$n=7$	$n=8$
1st	−0.87	−0.86	−0.86
2nd	−7.73	−7.81	−7.81
3rd	−5.65 + 24.25i	−16.2	−18.82 + 21.4i
4th	−5.65 − 24.25i	−16.3 + 13.09i	−18.82 − 21.4i
5th	−13.27 + 6.49i	−16.3 − 13.09i	−19.87 + 4.51i
6th	−13.27 − 6.49i	−3.21 + 34.5i	−19.87 − 4.51i
7th		−3.21 − 34.5i	0.814 + 46.2i
8th			0.814 − 46.2i

part, corresponding to the fluctuation shown in Fig. 13. From this figure, the truncated denominator polynomial guarantees a stable solution with an error of $<2\%$ for $n \leq 7$. For the calculations in this study, we find that $n = 4$ provides sufficient accuracy while being computationally efficient.

[1]C. Adachi, M. A. Baldo, M. E. Thompson, and S. R. Forrest, J. Appl. Phys. **90**, 5048 (2001).
[2]B. W. D'Andrade and S. R. Forrest, Adv. Mater. **16**, 1585 (2004).
[3]J. C. Sturm, W. Wilson, and H. Iodice, IEEE J. Sel. Top. Quantum Electron. **4**, 75 (1998).
[4]J. W. Park, D. C. Shin, and S. H. Park, Semicond. Sci. Technol. **26**, 034002 (2011).
[5]X. Qi, M. Slootsky, and S. Forrest, Appl. Phys. Lett. **93**, 193306 (2008).
[6]S. Chung, J.-H. Lee, J. Jeong, J.-J. Kim, and Y. Hong, Appl. Phys. Lett. **94**, 253302 (2009).
[7]C. Gärditz, A. Winnacker, F. Schindler, and R. Paetzold, Appl. Phys. Lett. **90**, 103506 (2007).
[8]L. A. Pipes, J. Franklin Inst. **263**, 195 (1957).
[9]W. R. LePage, *Complex Variables and the Laplace Transform for Engineers* (Dover, New York, 2010).
[10]H. Kim, C. M. Gilmore, A. Piqué, J. S. Horwitz, H. Mattoussi, H. Murata, Z. H. Kafafi, and D. B. Chrisey, J. Appl. Phys. **86**, 6451 (1999).
[11]H. Kim, A. Piqué, J. S. Horwitz, H. Mattoussi, H. Murata, Z. H. Kafafi, and D. B. Chrisey, Appl. Phys. Lett. **74**, 3444 (1999).
[12]S. R. Forrest, D. D. C. Bradley, and M. E. Thompson, Adv. Mater. **15**, 1043 (2003).
[13]V. Bulovic, V. B. Khalfin, G. Gu, P. E. Burrows, D. Z. Garbuzov, and S. R. Forrest, Phys. Rev. B **58**, 3730 (1998).
[14]I. Hatta and R. Codina, Comput. Methods Appl. Mech. Eng. **188**, 61 (2000).
[15]I. Hatta, Rev. Sci. Instrum. **50**, 292 (1979).
[16]E. Lemmon and R. Jacobsen, Int. J. Thermophys. **25**, 21 (2004).
[17]Y. Jin, A. Yadav, K. Sun, H. Sun, K. P. Pipe, and M. Shtein, Appl. Phys. Lett. **98**, 093305 (2011).
[18]K. Ramadan and M. A. Al-Nimr, In. J. Therm.l Sci. **48**, 1718 (2009).
[19]H. Benisty, R. Stanley, and M. Mayer, J. Opt. Soc. Am. A **15**, 1192 (1998).
[20]T. Matsushima and C. Adachi, Jpn. J. Appl. Phys. **46**, L861 (2007).
[21]L. A. Pipes, J. Franklin Institute **263**, 195 (1957).
[22]C. Zhang and G. Ding, Build. Environ. **38**, 699 (2003).
[23]W. H. Tanttila, Phys. Rev. Lett. **39**, 554 (1977).
[24]T. Yagi, K. Tamano, Y. Sato, N. Taketoshi, T. Baba, and Y. Shigesato, J. Vac. Sci. Technol. A **23**, 1180 (2005).
[25]H. Lee, Rev. Sci. Instrum. **53**, 884 (1982).
[26]T. E. Pochapsky, Acta Metallurgica **1**, 747 (1953).
[27]A. Woodcraft, Cryogenics **45**, 626 (2005).